Sensitive, 3D micromotion compensation in a surface-electrode ion trap

by

Amira M. Eltony

B.A.Sc., Engineering Physics
University of British Columbia (2010)

Submitted to the Department of Electrical Engineering
in partial fulfillment of the requirements for the degree of

Masters of Science in Electrical Engineering

at the

MASSACHUSETTS INSTITUTE OF TECHNOLOGY

September 2013

Author .....
Department of Electrical Engineering
August 30, 2013

Certified by.. .....
Isaac L. Chuang
Professor of Physics,
Professor of Electrical Engineering and Computer Science
Thesis Supervisor

Accepted by ....
Leslie Kolodziejski
Chairman, Department Committee on Graduate Students

Sensitive, 3D micromotion compensation in a surface-electrode ion trap

by

Amira M. Eltony

Submitted to the Department of Electrical Engineering
on August 30, 2013, in partial fulfillment of the
requirements for the degree of
Masters of Science in Electrical Engineering

Abstract

Following successful demonstrations of quantum algorithms and error correction with a handful of trapped ions in a macroscopic, machined Paul trap, there is a growing effort to move towards microfabricated traps with all the electrodes on a single chip. These traps, known as surface-electrode ion traps, are more amenable to being shrunk in size and replicated, or integrated with optical components and electronic devices. However, in the shift towards surface-electrode traps, and as traps are miniaturized in general, laser beams are brought closer to electrode surfaces, exacerbating laser-induced charging. Because of their charge, trapped ions are extremely sensitive to stray charges that accumulate on the trap surface. The DC potentials caused by stray charge displace the ion from the null of the RF trapping field, resulting in a fast, driven motion of the ion (known as micromotion) which hinders quantum operations by broadening transitions and causing decoherence.

In a surface trap, micromotion detection is difficult as the laser beams used for measurement typically cannot crash into the trap, obscuring ion offsets out of the trap plane. Existing methods for micromotion detection permit ion positioning accurate to the ground state wavepacket size (of order 10 nm), but cannot identify ion offsets out of the trap plane with the same accuracy. Schemes for sensitive compensation often have restrictive requirements such as access to a narrow atomic transition. We introduce a new approach, which permits out-of-plane micromotion compensation to within 10s of nanometers with minimal overhead. Our technique synchronously detects ion excitation along the trap axes when it is driven by secular-frequency sidebands added to the RF electrodes; the excitation amplitude is proportional to the offset from the RF null. We make a detailed theoretical comparison with other techniques for micromotion compensation and demonstrate our technique experimentally.

Thesis Supervisor: Isaac L. Chuang
Title: Professor of Physics, Professor of Electrical Engineering and Computer Science

Acknowledgments

A great thanks to Professor Isaac Chuang for giving me the opportunity to work in the Quanta Group and explore this exciting field. His generosity with his time and knowledge have been a huge help to me. Under his guidance, I have learned a great deal about designing and realizing scientific experiments, technical communication, and even management.

I have also gained immensely from interactions with Shannon Wang and Peter Herskind, who showed me the ropes of the cryogenic ion trapping experiment and introduced me to the lasers in lab during my first year in the group.

This work would not have been possible without the contributions of my talented co-workers. I'm grateful to David Meyer, who fabricated the ion traps in which the micromotion compensation experiments were performed, Rich Rines, who developed the photon counter hardware, Zachary Fisher, who helped with data taking, and Michael Gutierrez, who proposed the idea behind synchronous tickle measurement. I also benefitted greatly from knowledge shared through conversations with other members of the Quanta Lab, especially Molu Shi, Tony Kim and Hans Andersen.

Finally, thanks to my friends and family for their endless patience and support during this challenging process!

Contents

List of Figures

Chapter 1

Introduction

What happens when computers have shrunk down to just one atom per bit? At this scale, the bits behave according to quantum mechanics, and a new model of computation, "quantum computation", becomes possible, expanding capabilities for simulation and for new (and in some cases, more-efficient) algorithms. Physics experiments with single atomic ions acting as "quantum bits" have demonstrated many of the ingredients for a quantum computer. But, to perform useful computations these experimental systems will need to be vastly scaled-up.

By building on established techniques of microfabrication, surface-electrode ion traps offer a potential route to scalability, but also present a number of challenges. This thesis focuses on one particular challenge: compensating micromotion in a surface-electrode trap geometry, where the proximity of laser beams parallel to the trap surface exacerbates charge build-up and at the same time makes detection difficult. This first chapter reviews progress towards quantum computation with trapped ions and puts the problem of sensitive micromotion detection in context.

1.1 Quantum computing with ions

A quantum computer is a machine that performs calculations through the control and manipulation of quantum objects. Harnessing properties of quantum mechanics such as entanglement and superposition, a quantum computer can simultaneously

follow multiple computation paths, allowing interference of these paths to produce a result. For certain problems, like factoring large numbers into primes [Sho94] or searching large databases [Gro96], quantum algorithms exist which are significantly more efficient than the best known classical algorithms as the size of the problem increases. Motivated by these applications, the first quantum computers consisting of only a handful of quantum bits (qubits) have been developed in a variety of physical systems, among them: nuclear spins of molecules in liquid solution (NMR) [VSB+00], optical photons [PMO09], superconducting circuits [RDN+12], semiconductor quantum dots [PJT+05], neutral atoms [IUZ+10], and atomic ions [MKH+09]. So far, trapped ion qubits are leading the pack, owing to their their long lifetimes (single ions can remain confined in a Paul trap for hours or days), long coherence times (ranging from ms to s) relative to the gate times (typically μs or less), strong inter-ion interactions (via the Coulomb force), and natural reproducibility (to the best of our knowledge, all $^{88}Sr^{+}$ ions are identical).

A complete methods set for scalable quantum computing with ions has been described [HHJ+09] and toy computers based on trapped ion qubits have provided proof-of-principle demonstrations of the essential ingredients [DiV95], including: high-fidelity quantum state preparation [RZR+99, MMK95b, KWM+98], single qubit rotations [RZR+99, NLR+99], multi-qubit operations [MMK95a, SKK+00, LDM+03, SKHR+03, MKH+09], and state read-out [RZR+99, RKMS01, MSW+08]. Demonstrations of quantum algorithms including the Deutsch-Josza algorithm [GRL+03], the quantum Fourier transform [CBL+05], and Grover search [BHL+05] have been achieved with a few trapped ions. Recently, quantum error correction was also demonstrated with ions [SBM+11], but it is a formidable technical challenge to extend these results much beyond the current experimental record of 14 qubits [MSB+11]. In these demonstrations, the qubits are chains of ions trapped in machined 4-rod style Paul traps (as shown in Figure 1-1), which are likely limited to computations with 10s of ions [WMI+98].

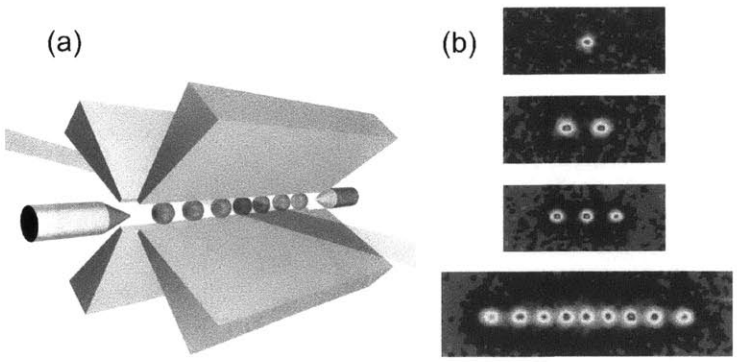

Figure 1-1: (a) Schematic of a Paul trap consisting of four RF electrodes and two end-cap (DC) electrodes to confine ions in a linear chain. A laser beam is shown applying a gate pulse to a single ion. (b) Camera images of few ions in a Paul trap. The spacing between ions is approximately 5 μm. Images courtesy of University of Innsbruck.

1.2 Scaling-up ion traps

Surface-electrode Paul traps, in which ions are trapped 30 to 200 μm above a planar chip, take advantage of well-developed techniques of microfabrication to make ion traps miniaturizable and more reproducible [SHO+05, SCR+06]. A typical surface-electrode ion trap is pictured in Figure 1-2. Building on this technology, a large-scale quantum computer could potentially be constructed by interconnecting a large number of ion traps to form a "quantum charge-coupled device" (QCCD) [KMW02]. In such an architecture, a few interacting ions are confined in each trap, and gates are performed between the traps by shuttling ions between the different trap zones, as pictured in Figure 1-3. However, there are major challenges to scaling-up surface-electrode traps to confine dense arrays of ions. Foremost, is the presence of increasing electric field noise as ions are brought close to the electrode surface, which limits gate fidelity and coherence time [TKL+00]. As traps are miniaturized, laser beams are also brought closer to electrode surfaces, exacerbating laser-induced charging of the trap [WHL+11]. The DC potentials caused by stray charge displace the ion from the RF electric field null, resulting in a fast driven motion of the ion (called "excess micromotion"), which is detrimental because it broadens transitions and can cause decoherence [BM98]. Stray charge can be detected and its effect cancelled

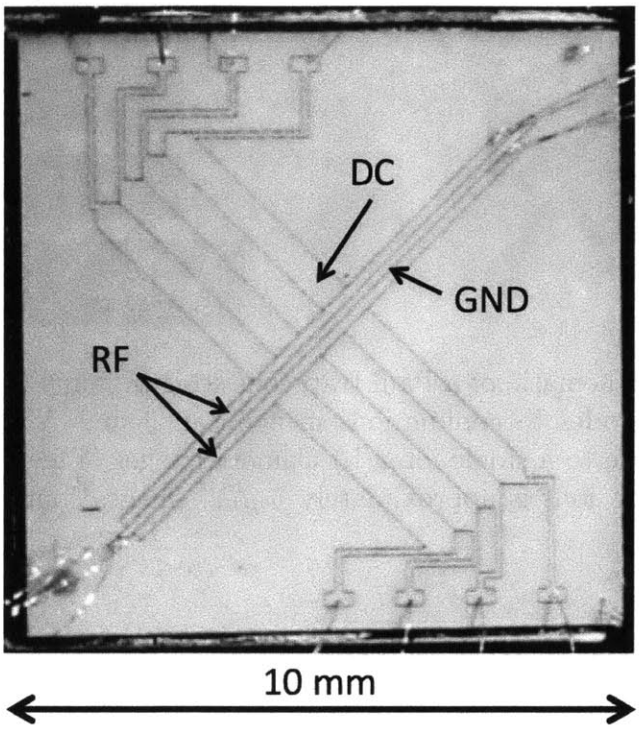

Figure 1-2: Photograph showing a typical surface-electrode ion trap (with copper electrodes fabricated on quartz substrate). In this trap, ions are confined 150 μm above the center ground electrode in a location defined by the DC electrode voltages. For more details, see Figure 2-1.

by applying corrective DC voltages to the trap electrodes (known as "compensating micromotion"). But, detecting stray charge is difficult in a planar trap because the laser beams used for measurement typically cannot have a projection out of the trap plane, meaning that ion displacements out of the plane are not easily identified. Addressing this challenge - precise compensation of micromotion in a surface-electrode trap geometry - is the focus of this thesis.

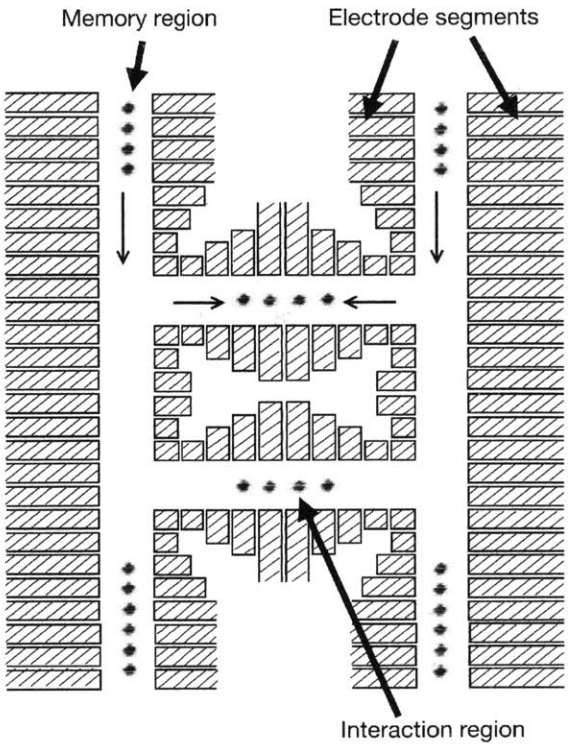

Figure 1-3: Diagram of the quantum charge-coupled device (QCCD). Ions are stored in the memory region and moved to the interaction region for logic operations. Thin arrows show transport and confinement along the local trap axis. Reproduced from Ref. [KMW02].

1.3 Effects of micromotion

Micromotion is the driven motion of an ion displaced from the zero-point of the AC trapping field. The ion can be displaced by phase offsets between trap electrodes, but is affected more by stray electric fields. Such fields readily build-up from charge deposition onto the trap during ion loading [BLW+07], or photoelectric charge creation from laser fields [WHL+11]. The resulting micromotion broadens and shifts atomic transitions [BM98], leaks in noise from the RF source, and interferes with ion coupling to integrated trap elements such as optical fibers [KHC11]. For multiple co-trapped ions, the micromotion of one ion can result in parametric heating of the secular motion of another ion [RZS05, BKQW89, DHB89], which is detrimental to experiments with ion crystals, or sympathetic cooling schemes (for a single ion, the micromotion and the secular motion are strongly decoupled, so micromotion does

not usually result in direct heating of the secular motion). For an ion sympathetically cooled using cold atoms, micromotion can cause heating of the ion's secular motion through long-range ion-atom collisions [CGV12]. Micromotion build-up is exacerbated as traps are miniaturized, placing the ion and laser beams nearer to trap electrodes and dielectric materials. Precise compensation of stray electric fields is essential to applications of trapped ions ranging from stable frequency standards to ultra sensitive force detectors to qubits.

Compensating micromotion is placing the ion at the null of the RF quadrupole field by precise corrections to the DC trap voltages. Better compensation is achieved by positioning the ion closer to the null. For example: to assure that the Doppler-cooling transition (with $\Gamma \approx 20$ MHz at 422 nm for $^{88}Sr^{+}$) is broadened by less than 1% by micromotion, the ion must be positioned to within ≈ 0.7 μm of the RF null (assuming the secular frequency $\omega_x = 1$ MHz and the RF frequency $\Omega_{RF} = 35$ MHz). Likewise, to guarantee that the strength of the carrier transition used for qubit rotations is reduced by less than 1% by micromotion, the ion must be within ≈ 400 nm of the RF null (assuming the linewidth of the transition is $\Gamma \approx 100$ kHz at 674 nm). Stricter constraints on compensation arise when the ion is to be coupled to integrated optical elements, or positioned within a cavity standing wave; in this case, the micromotion amplitude must be a fraction of the optical wavelength (order 10s of nanometers).

1.4 Compensating micromotion

Coarse compensation of micromotion can be achieved by choosing DC voltages to minimize broadening of a fairly wide (order 10 MHz linewidth) atomic transition due to micromotional sidebands [Roo00]. Alternatively, the change in ion position with scaling RF field strength can be detected, for example on a CCD camera, or by monitoring the distance a focused laser beam must be translated to maintain maximum photon scattering from the ion. The trap DC voltages can then be corrected until the ion does not move with changing RF amplitude [BM98]. This allows micromo-

tion compensation to the accuracy of laser beam positioning or the resolution of the imaging system, typically corresponding to placing the ion within ≈ 1 μm of the RF null. The main drawback of this technique is that it is not sensitive to micromotion caused by a phase offsets between electrodes.

Finer compensation is possible using resolved sideband spectroscopy on a narrow atomic transition. Here, micromotion is measured by comparing the Rabi frequency of the first micromotional sideband to that of the carrier [Roo00]. This technique allows ion positioning accurate to the ground state wavepacket size (of order 10 nm), but requires access to a narrow atomic transition, which is technically challenging and costly. A simpler compensation scheme not requiring a narrow transition, relies on detection of ion motion correlated with the RF drive. Here, micromotion induces a varying Doppler shift of the incoming cooling beam over the RF cycle, varying the detuning from resonance, which produces a modulation of the fluorescence at the RF frequency [BM98]. This scheme also allows ion positioning accurate to 10s of nanometers.

Both the resolved sideband and the RF correlation measurement approaches can provide nanometer sensitivity, but they only allow detection of micromotion with a projection onto the laser beam (unless the RF trapping potential is tilted, which is typically not the case). For a microtrap geometry, where crashing the beam into the surface would result in undesirable charging and background light scattering, this proscribes detection of micromotion out of the trap plane. This obstacle can be circumvented with a $^{40}Ca^{+}$ ion by angling an infrared (IR) repump laser, less likely to cause photoemission and charging of the trap substrate, into the trap and using a coherent Raman process to detect micromotion in all directions[ASS+10]. The resulting ion positioning resolution is nearly as good as for the RF correlation technique. Unfortunately, this scheme is limited to ions with infrared transitions.

A more general approach detects displacement of the ion from the RF null through the electric field of an additional voltage applied to the RF electrodes. If the added voltage has a frequency component in resonance with one of the trap frequencies, the ion will be excited along this trap axis. Exciting the ion by applying a voltage

with a frequency component equal to a trap frequency is known as "tickling" the ion. For a large enough ion offset from the null, the amplitude of the ion's driven motion will cover a significant portion of the Doppler cooling beam waist, affecting the cooling rate and resulting in a detectable change in fluorescence [NDM+11, TMA+11]. Provided the radial trap axes are tilted (which can readily be achieved in a planar trap using the DC potential), out of plane compensation is possible. The excitation voltage can be increased to improve the accuracy of this technique, up to the limit where the amplitude of the ion's motion take it outside of the trapping volume, and it is lost. A positioning resolution of 300 nm has been demonstrated using this approach [NDM+11].

The different techniques for micromotion detection are summarized in Table 1.1, including our proposed technique.

Micromotion measurement technique	Ion positioning resolution	Out-of-plane detection possible?	Significant disadvantages
ion displacement with RF amplitude variation	≈ 1 μm	yes	insensitive to micromotion caused by phase offsets between electrodes
resolved sideband spectroscopy	40 nm [Roo00]	no [a]	access to a narrow transition required
RF correlation measurement	30 nm [ASS+10]	no [a]	
RF correlation measurement with angled IR laser	70 nm [ASS+10]	yes	limited to ions with IR transitions
excitation voltage on RF electrodes	300 nm [NDM+11]	yes	
synchronous tickle measurement	order 10 nm [b]	yes	

[a] Typically (unless the RF trapping potential is tilted)
[b] In theory (not experimentally verified)

Table 1.1: Comparison of different techniques for micromotion detection. See the text for a description of each technique. Unless noted otherwise, the ion positioning resolution is an experimentally determined value.

1.5 Our approach: synchronous tickle detection

By making a correlated measurement (similar to the RF correlation technique described above) while exciting the ion along one of the trap axes through the RF electrodes, we combine the ability to compensate micromotion out of the trap plane with high sensitivity, without the requirement for access to a narrow atomic transition or other costly equipment. Our technique adds sidebands to the RF voltage at one of the radial trap frequencies, and then detects fluorescence with a definite phase relationship to the added voltage. Similarly to the RF correlation technique, the driven motion of the ion at the trap frequency results in a modulation of the fluorescence at this frequency via the Doppler shift of the incident beam. The closer the ion is to the field null, the smaller the driving force, and hence the smaller the correlated scattering rate. We call this the "synchronous tickle" measurement technique for micromotion detection. Combined with the RF correlation technique for micromotion compensation in-plane, our technique allows for sensitive, 3D micromotion compensation in a surface-electrode ion trap. A related technique has been employed for high resolution mass spectrometry of single molecular ions [DMM+04].

In order to put our approach in context, we make a detailed comparison with other possible techniques for compensation to within the ground state wavepacket size in Chapter 2. Then, we demonstrate this new technique experimentally in Chapter 3. Our investigations focus on microfabricated, surface-electrode ion traps operated in a bath cryostat (at 4 K and 77 K), where low pressure is achievable within a short time frame, and heating of the ion's motional state is suppressed [LGA+08].

Chapter 2

Comparison of sensitive compensation techniques

This chapter presents the theory describing synchronous tickle measurement. We begin with a brief introduction to surface-electrode ion traps. For comparison, some alternative approaches: the resolved sideband and the RF correlation techniques, are also described. Like synchronous tickle measurement, these techniques allow micromotion compensation to within the ground state wavepacket size of the trapped ion (of order 10 nm). A summary of the advantages and disadvantages of these techniques can be found in Table 2.1.

Micromotion measurement technique	Out-of-plane compensation possible?	Compensation without access to narrow transition?	Integration time required for 10 nm positioning accuracy
resolved sideband	no [a]	no	40 ms
RF correlation	no [a]	yes	300 ms
synchronous tickle	yes	yes	6 ms [b]

[a] Typically (unless the RF trapping potential is tilted)
[b] Assuming $V_{tickle} = 1$ V

Table 2.1: Comparison of different techniques for sensitive micromotion compensation. The integration times compared are those required for $> 99\%$ confidence that the ion is within 10 nm of the RF null, for typical experimental settings. (The secular frequency is assumed to be: $\omega_x = 1$ MHz).

2.1 Surface-electrode ion traps

The quadrupole potential providing confinement in a Paul trap can be produced by a combination of two-dimensional RF and DC electrodes [CBB+05], known as a "surface-electrode" (or "planar") ion trap. A generic surface-electrode trap is pictured in Figure 2-1, along with the coordinate system used throughout this work. The central three RF electrodes provide confinement in the radial directions (the x and y directions), and the outer DC electrodes add confinement in the axial direction (the z direction). Typically, an ion is trapped on the order of 100 μm above the surface. Laser access is restricted in a surface-electrode trap geometry as lasers are constrained to lie in a plane parallel to the trap. But, the symmetry of the surface-trap geometry can be explicitly broken using either the electrode shapes themselves or the DC voltages applied so that all of the principal trap axes have a projection onto the cooling laser beam.

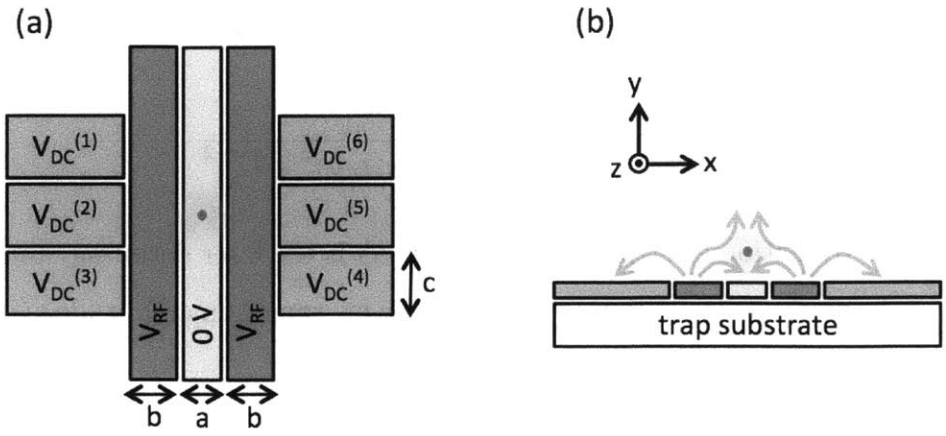

Figure 2-1: (a) A generic surface-electrode ion trap electrode geometry. When $V_{DC}{}^{(1)} = V_{DC}{}^{(3)} = V_{DC}{}^{(4)} = V_{DC}{}^{(6)}$ is positive, and $V_{DC}{}^{(2)} = V_{DC}{}^{(5)}$ is negative, a symmetric trap is formed with the ion trapped above the surface at the center (indicated in blue). The trap dimensions, a, b, c are typically chosen to optimize properties such as the trap depth. (b) A cross-sectional view of the trap showing electric field lines and the coordinates used in the text.

2.2 Resolved sideband measurement

If we have access to a narrow atomic transition (such as the $5S_{1/2} \leftrightarrow 4D_{5/2}$ quadrupole transition in $^{88}Sr^{+}$) sensitive micromotion detection is possible using resolved sideband spectroscopy. By comparing the Rabi frequencies (or scattering rates) of the carrier transition and the first micromotional sideband, the micromotion amplitude is extracted [BM98]. This technique has the advantage of allowing for nanometer-scale micromotion compensation, but the requirement of access to a narrow transition is restrictive and 3D compensation is not possible unless the RF trapping potential is tilted.

In the ion's reference frame, micromotion corresponds to a frequency modulation of the laser light at the RF frequency. This converts the Lorentzian excitation spectrum of the ion into a sum of Lorentzians peaked at $\omega_0 \pm n\Omega_{RF}$ (where ω_0 is the atomic transition frequency, and Ω_{RF} is the RF frequency). This is illustrated in Figure 2-2. In the low-saturation limit, the excited state population can be written using a Bessel

function expansion [DHB89]:

$$\rho_{ee}(\Delta) = \frac{\chi^2}{4} \sum_{n=-\infty}^{+\infty} \frac{J_n(\beta)^2}{(\Delta - n\Omega_{RF})^2 + \left(\frac{\Gamma}{2}\right)^2} \tag{2.1}$$

Here, χ is the transition electric dipole moment, Δ is the laser detuning, and Γ is the (saturation broadened) transition linewidth. The micromotion amplitude is described by the modulation index β:

$$\beta = kx_{amp} = k\sqrt{2}\frac{\omega_x}{\Omega_{RF}}x_d \tag{2.2}$$

(where x_{amp} is the amplitude of micromotion, x_d is the ion displacement from the RF null, and $k = \frac{2\pi}{\lambda}$ is the wave number). Hence, by comparing the Rabi frequency with the laser tuned to the carrier transition, Ω_0, with the Rabi frequency when the laser is tuned to the first micromotional sideband, Ω_1, the modulation index, β, is measurable:

$$\frac{\Omega_1}{\Omega_0} = \frac{J_1(\beta)}{J_0(\beta)}. \tag{2.3}$$

In the limit of small modulation, this expression simplifies to

$$\frac{J_1(\beta)}{J_0(\beta)} \approx \frac{\beta}{2}. \tag{2.4}$$

Typical carrier π times are close to 5 μs (not shorter to avoid excessive power broadening, which increases off-resonant carrier transitions and limits coherence time) [WLG+10]. For an ion displaced from the RF null by 10 nm, the modulation index is about $\beta = 0.004$, resulting in an effective π time of $\frac{2}{\beta}(5\ \mu s) = 2.7$ ms for the first micromotional sideband. To remain well within the coherence time, we may choose to make state detection measurements following a $\pi/3$ pulse (in this case, after $\approx 880\ \mu$s), at which time the transition probability is expected to be 1/2. By repeating this measurement many times, we can measure the transition probability

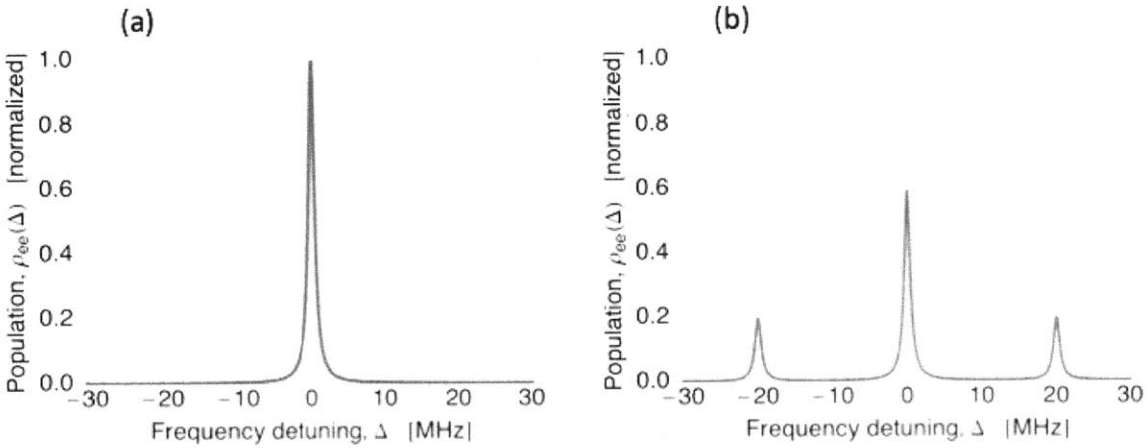

Figure 2-2: Computed plots showing the excited state population, $\rho_{ee}(\Delta)$, for an example transition with a linewidth of $\Gamma = 1$ MHz, for different values of the micromotional modulation index β. The population is normalized to the value at zero-detuning, $(\chi/\Gamma)^2$, and the RF frequency is set to 20 MHz. (a) $\beta = 0$ (no micromotion) (b) $\beta = 1$ (significant micromotion)

experimentally, which allows us to determine the modulation index via:

$$Pr(|0\rangle \rightarrow |1\rangle) = \sin^2\left[\frac{\beta}{2}\left(\frac{\Omega_0 t}{2}\right)\right]. \tag{2.5}$$

Assuming that we take a few 100 μs for state-readout, measurement error can be neglected and the uncertainty comes from counting statistics. Hence, if we want to ascertain that the ion is within 10 nm of the RF null (accurate to 3σ), we would need to perform $\approx N$ trials, where N is given by

$$N = \frac{3^2}{\sin^4\left[\frac{\beta}{2}\left(\frac{\Omega_0 t}{2}\right)\right]} \approx 40. \tag{2.6}$$

If each trial takes ≈ 1 ms (including state initialization, the $\pi/3$ pulse, and read-out), this corresponds to a total measurement time of ≈ 40 ms.

2.3 RF correlation measurement

A simpler compensation scheme, not requiring a narrow transition, relies on detection of ion motion correlated with the RF drive. Here, micromotion induces a varying

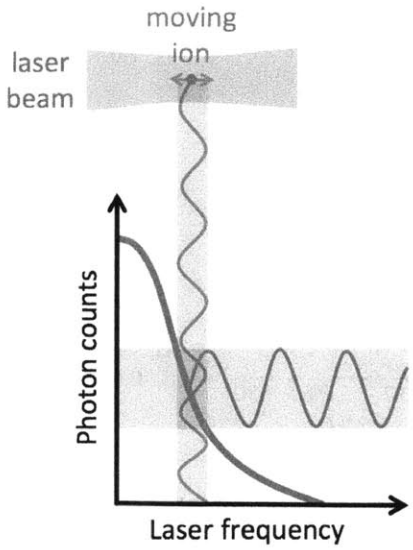

Figure 2-3: Conceptual illustration of the RF correlation technique for micromotion detection. Micromotion (movement of the ion at the RF frequency) translates into oscillation of the laser frequency (as seen by the ion) at the RF frequency, and hence results in oscillation in the fluorescence rate at the RF frequency.

Doppler shift of an incoming cooling beam over the RF cycle, varying the detuning from resonance, which produces a modulation of the fluorescence rate at the RF frequency. A conceptual illustration of this can be found in Figure 2-3. This approach can provide nanometer sensitivity without requiring access to a narrow transition, but only allows detection of micromotion with a projection onto the laser beam.

Detection is performed using photons scattered on the Doppler cooling transition. The scattering rate is given by:

$$R = \Gamma \rho_{ee} \tag{2.7}$$

where Γ is the natural linewidth of the transition, and ρ_{ee} is the excited state probability. An ion undergoing micromotion sees a Doppler shift of the incoming laser frequency by [BM98] $\beta\Omega_{RF}\sin(\Omega_{RF}t+\delta)$, resulting in a fluorescence rate of

$$R(t) = \frac{\Gamma\Omega^2}{\Gamma^2 + 4(\Delta - \beta\Omega_{RF}\sin(\Omega_{RF}t+\delta))^2} \tag{2.8}$$

(in the low intensity limit) where $\Delta = \omega_L - \omega_0$ is the detuning of the laser, and $\Omega = \Gamma\sqrt{\frac{I}{2I_{sat}}}$ is the Rabi frequency. The modulation index β is as defined above.

Assuming that we choose $\Delta = -\frac{\Gamma}{2}$ for optimal Doppler cooling, this becomes

$$R(t) = \frac{\Gamma\Omega^2}{\Gamma^2 + 4(\frac{\Gamma}{2} - \beta\Omega_{RF}\sin(\Omega_{RF}t + \delta))^2}. \tag{2.9}$$

In the limit that $\beta\Omega_{RF} \ll \Gamma$, this is approximately

$$R(t) \approx \frac{\Omega^2}{2\Gamma} + \frac{\Omega^2}{\Gamma^2}\beta\Omega_{RF}\sin(\Omega_{RF}t + \delta). \tag{2.10}$$

So, the average count rate R_{avg} will be unchanged (to first order) with the excess micromotion:

$$R_{avg} = \frac{\Omega^2}{2\Gamma}, \tag{2.11}$$

and the component of scattered photons correlated with the RF drive will have amplitude:

$$R_{corr} = \frac{\Omega^2}{\Gamma^2}\beta\Omega_{RF}. \tag{2.12}$$

The observed count (at the photodetector), $n = \eta R_{avg}\tau$ (where η is the light collection efficiency, R_{avg} is the average count rate and τ is the integration time), follows Poisson statistics. So, the expected variation in counts goes as

$$\Delta n = \sqrt{\eta R_{avg}\tau} = \sqrt{\frac{\eta\tau\Omega^2}{2\Gamma}}. \tag{2.13}$$

Thus, if we want to be confident (to 3σ) that the ion is within 10 nm of the RF null (corresponding to $\beta = 0.006$), we need an integration time of approximately

$$\tau = \left(3^2\frac{\sqrt{\eta R_{avg}}}{\eta R_{corr}}\right)^2 = \left(\sqrt{\frac{\Gamma^3}{2\eta\Omega^2}}\frac{9}{\beta\Omega_{RF}}\right)^2. \tag{2.14}$$

For the Doppler cooling transition at 422 nm in $^{88}Sr^+$, the linewidth, $\Gamma \approx 20$ MHz. For typical experimental settings (light collection efficiency $\eta = 1\%$, secular frequency $\omega_x = 1$ MHz), this corresponds to ≈ 300 ms integration time.

2.4 Synchronous tickle measurement

Our method allows for detection of micromotion out of the trap plane in a surface trap (with a DC tilt of the trap axes), by tickling the ion (applying a voltage in resonance with one of the secular frequencies) through sidebands added to the RF trapping voltage. Unless the ion is at the RF null, it will undergo driven motion whose scale is determined by the distance from the null. This driven motion of the ion at the trap frequency results in a modulation of the fluorescence rate via the Doppler shift of the incident beam, which has a fixed phase relationship to the drive source used to generate the sidebands. Hence, a correlation measurement is possible similar to the RF correlation technique described above. This technique has both the advantage of not requiring access to a narrow transition, and allowing for nanometer-scale micromotion compensation in all trap directions.

Assume that we apply a small voltage at the tickle frequency to the RF electrodes (for example by adding sidebands to the trap RF signal at the tickle frequency). Near the RF null, the (time-averaged) tickle potential is well-approximated by a 2D quadratic well. In one of the trap directions ($\hat{x}$), this corresponds to an electric field of the form

$$E_x(x) = \frac{m\omega_{eff}^2 x}{e}. \tag{2.15}$$

Here, ω_{eff} is an effective trap frequency for the component of the potential at the tickle frequency:

$$\omega_{eff} = \kappa \frac{V_{tickle}}{\omega}, \tag{2.16}$$

and κ is a factor including both a geometric factor (depending on the dimensions of the RF electrodes) and some constants (mass, e, factors of 2, etc.). An approximate analytic model for the electric field of the RF electrodes [Hou08] can be used to estimate κ for a given trap geometry. Hence, if a stray electric field displaces the ion a distance x_d in the $\hat{x}$ direction from the RF null, the resulting tickle drive force is (approximately)

$$F_d(x_d) = m\omega_{eff}^2 x_d = m\left(\frac{\kappa V_{tickle}}{\omega}\right)^2 x_d. \tag{2.17}$$

Because the tickle frequency (close to the secular frequency) is much less than the RF frequency, we can treat the trap as stationary. For simplicity, consider a single trap mode (1-d harmonic oscillator). Described classically, the equation of motion for this damped harmonic oscillator under periodic force is

$$\ddot{x} + 2\gamma\dot{x} + \omega_x^2 x = \frac{F_{drive}(t)}{m}, \tag{2.18}$$

where ω_x is the trap secular frequency, $\gamma = \frac{\hbar\Omega^2 k^2}{2m\Gamma^2}$ is the damping coefficient due to Doppler cooling, and m is the ion mass. The tickle drive provides the external forcing function: $F_{drive}(t) = F_d \cos(\omega t)$. In general, the solution to this second order ODE will be made up of a particular solution, which is periodic in time with the same period as the driving force, and a solution to the corresponding homogeneous equation which will decay exponentially in time (the transient term). Since the transient will die away at a rate γ, (≈ 40 kHz) this term can be neglected for integration times typical in practice. So, the driven motion of the ion can be written as:

$$x(t) = A(\omega)\cos(\omega t - \theta(\omega)), \tag{2.19}$$

where the amplitude is given by

$$A(\omega) = \frac{F_d/m}{\sqrt{(\omega_x^2 - \omega^2)^2 + 4\gamma^2\omega^2}}, \tag{2.20}$$

and the phase is given by

$$\tan(\theta(\omega)) = \frac{2\gamma\omega}{\omega_x^2 - \omega^2}. \tag{2.21}$$

Detection is performed using photons scattered on the Doppler cooling transition. The scattering rate is given by

$$R = \Gamma\rho_{ee} \tag{2.22}$$

We can linearize ρ_{ee} around zero velocity, to obtain

$$R = \frac{\Omega^2}{2\Gamma} + \frac{\Omega^2 k}{\Gamma^2}\dot{x}, \tag{2.23}$$

(assuming that we choose $\Delta = -\frac{\Gamma}{2}$ for optimal cooling). Substituting in the expression for $x(t)$ to $\dot{x}$ we obtain the scattering rate as a function of time:

$$R(t) = \frac{\Omega^2}{2\Gamma} - \frac{\omega\Omega^2 k A(\omega)}{\Gamma^2}\sin(\omega t - \theta(\omega)) \tag{2.24}$$

(for $A(\omega)$ and $\theta(\omega)$ defined above). So, the average count rate R_{avg} will be unchanged (to first order) with the excess micromotion:

$$R_{avg} = \frac{\Omega^2}{2\Gamma}, \tag{2.25}$$

and the component of scattered photons correlated with the tickle drive will have amplitude:

$$R_{corr}(\omega) = \frac{\omega\Omega^2 k A(\omega)}{\Gamma^2} = \frac{\omega\Omega^2 k F_d}{m\Gamma^2\sqrt{(\omega_x^2 - \omega^2)^2 + 4\gamma^2\omega^2}}. \tag{2.26}$$

The resulting phase is simply the phase offset $\theta(\omega)$ of the driven motion of the ion from the tickle drive source, which is given by

$$\tan(\theta(\omega)) = \frac{2\gamma\omega}{\omega_x^2 - \omega^2}. \tag{2.27}$$

The expected tickle signal for a typical experimental situation is shown in Figure 2-4.

At the photodetector, the observed count $n = \eta R_{avg}\tau$, (where η is the light-collection efficiency, R_{avg} is the average count rate and τ is the integration time), follows Poisson statistics. So, the expected variation in counts goes as

$$\Delta n = \sqrt{\eta R_{avg}\tau} = \sqrt{\frac{\eta\tau\Omega^2}{2\Gamma}} \tag{2.28}$$

As before, if we want to be confident (to 3σ) that our ion is within distance x_d of the RF null, we need an integration time of approximately

$$\tau = \left(3^2\frac{\sqrt{\eta R_{avg}}}{\eta R_{corr}}\right)^2 = \left(\frac{9\hbar\Omega k}{\sqrt{2\Gamma\eta}F_d}\right)^2 = \left(\sqrt{\frac{\hbar^2\Omega^2}{\eta\Gamma}}\frac{9k^2\omega_x^3}{\beta\Omega_{RF}\kappa^2 m V_{tickle}^2}\right)^2 \tag{2.29}$$

(assuming that we are driving on resonance: $\omega = \omega_x$) For $x_d = 10$ nm (corresponding

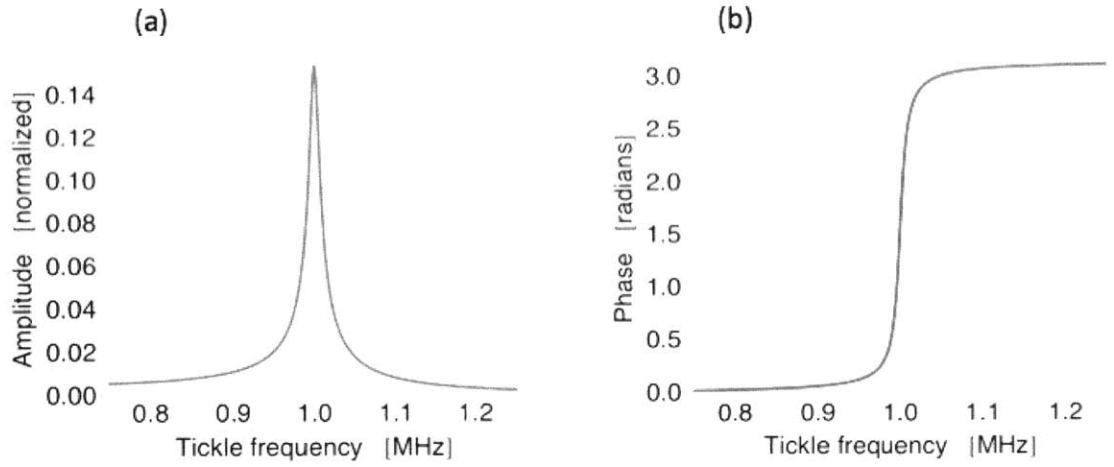

Figure 2-4: Computed synchronous tickle signal for an ion offset by 10 nm from the RF null, driven by a tickle voltage of 1 V. The trap and experimental parameters used are similar to those in our experiments with $^{88}Sr^{+}$ (wavelength of 422 nm, transition linewidth of 20 MHz, secular frequency of 1 MHz). (a) Signal amplitude (ratio of correlated scattering rate to total scattering rate) (b) Signal phase

to $\beta = 0.006$), and tickle voltage of 1 V applied, this is about 6 ms (for the Doppler cooling transition at 422 nm in $^{88}Sr^{+}$, with linewidth, $\Gamma \approx 20$ MHz, and assuming light collection efficiency $\eta = 1\%$, secular frequency $\omega_x = 1$ MHz).

Chapter 3

Experimental synchronous tickle measurement

This chapter describes efforts to verify the synchronous tickle measurement technique experimentally with a single $^{88}Sr^{+}$ ion confined 150 μm above a surface-electrode ion trap. The experimental system in which this work was undertaken, a 4 K bath cryostat, is briefly introduced along with the specific apparatus required for micromotion compensation. Lastly, we discuss limitations to the measurement sensitivity achievable in this system.

3.1 Trap geometry and fabrication

The surface-electrode trap geometry chosen for this work is pictured in Figure 3-1. The two RF electrodes are directly connected together. The relative sizes of the electrodes are chosen such that the ratio of the RF electrode width to the ground electrode width is ≈ 1.19, which maximizes the trap depth. The absolute electrode widths are chosen to set a trap height of ≈ 150 μm, which is convenient for laser access to the ion. The length of the RF electrodes is chosen to be as long as possible (to minimize edge effects that would create micromotion in the axial direction), while not so long that the trap capacitance becomes very high (making it difficult to drive RF using a resonator).

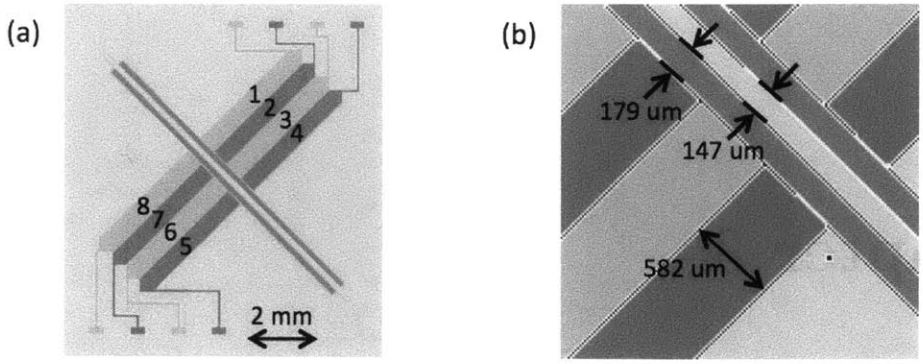

Figure 3-1: (a) Schematic showing the trap electrode geometry. The RF electrodes are shown in red, the ground electrodes are shown in blue, and the eight DC electrodes are shown in green. (b) The central trapping region with key dimensions indicated (for an ion height of about 150 μm). Dimensions are shown net of gaps between electrodes (which are 15 μm).

For this work, the electrode material was 100 nm of niobium. The trap was patterned starting with optical lithography using PR1-2000A photoresist on sapphire substrate. Next, niobium was deposited by RF sputtering with argon gas at a rate of 0.8 Å/s at low pressure (1.5 mTorr) and high temperature (200 °C). Finally, the resist pattern was transferred to the niobium via lift-off with RD6. An additional reactive-ion etching step in carbon tetrafluoride and oxygen gas for 10 minutes was added to remove residue from the trap surface. The packaged ion trap can be seen in Figure 3-2; there are some additional DC electrodes (different from Figure 3-1) which were not used.

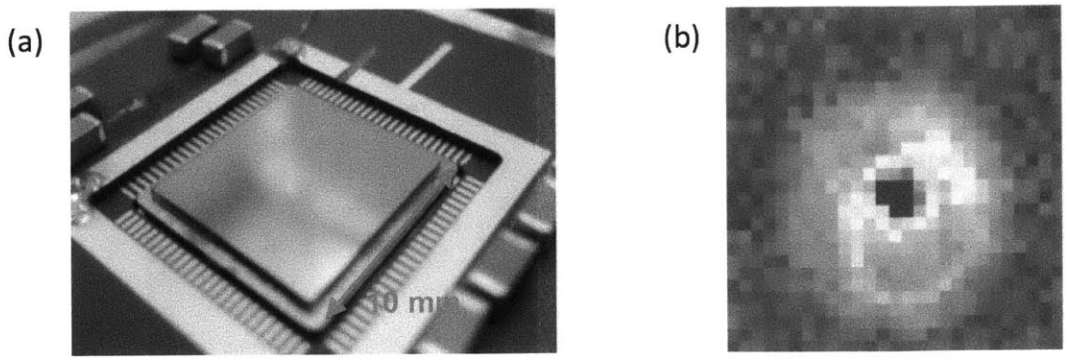

Figure 3-2: (a) Photograph showing the surface-electrode ion trap employed in this work. The trap is mounted in a 100-pin, ceramic pin grid array (CPGA) chip carrier and wirebonded to provide electrical connections to the electrodes. (b) A single, trapped $^{88}Sr^{+}$ ion as seen on the experiment CCD camera. The camera image shows a region of approximate size: 50 μm $\times$ 50 μm.

3.2 Cryogenic experiment

The ion trap is operated at cryogenic temperature (4 K or 77 K), where low pressure is achievable within a short time frame and heating of the ion's motional state is suppressed [LGA+08]. To achieve this, the trap and other required components are mounted to the 4 K baseplate of a commercial liquid helium bath cryostat (QMC Instruments Model TK 1813), as depicted in Figure 3-3. There are three viewports on the chamber, allowing laser access to the trapping region, and one 55-pin electrical feedthrough. The base pressure at room temperature is only $\approx 10^{-6}$ Torr, but cryosorption, aided by two activated charcoal adsobers (mounted on the helium baseplate and at the top of the nitrogen shield to increase the effective surface area), results in sufficiently low pressure (estimated to be $\approx 10^{-12}$ Torr [Bak06] in this system) for stable trapping. A filter board containing low-pass filters (2nd order, 4 kHz corner frequency) for each of the DC electrodes is heat sunk to the 4 K baseplate. To reduce the heat load on the LHe tank, the neutral oven (used to produce a beam of neutral Sr atoms at the trap site for subsequent photoionization and loading) and the helical resonator (used to step-up the RF trap voltage) are thermally anchored to the 77 K shield. Further details about the construction of the cryostat can be found in Ref. [ASA+09] and Ref. [Bak06].

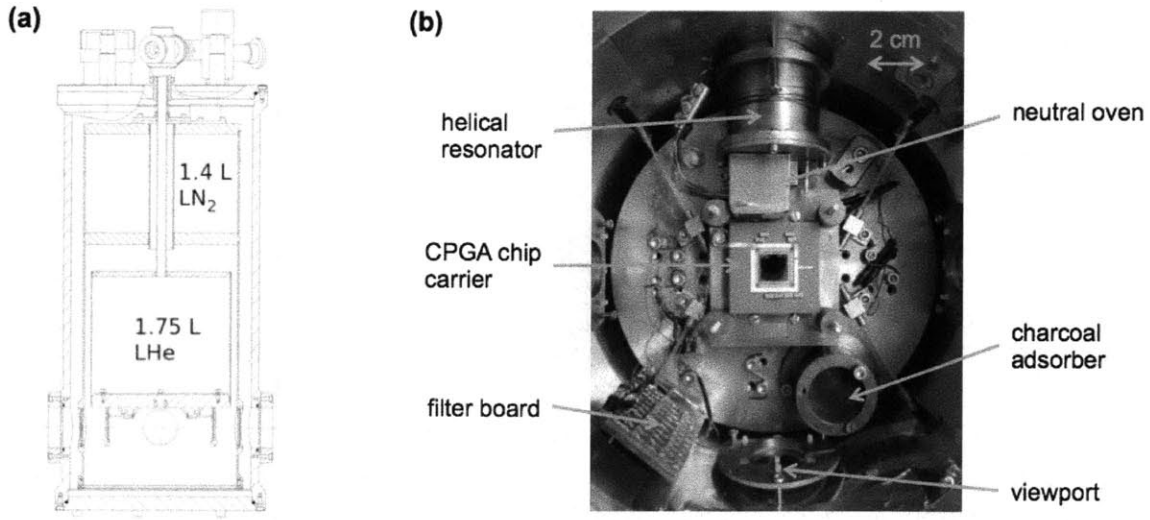

Figure 3-3: (a) Schematic of the bath cryostat, with liquid helium (LHe) and liquid nitrogen (LN_2) tanks labeled. The 77 K shield attached to the LN_2 tank encloses the LHe tank and the 4 K baseplate. The working area (where the trap is mounted) is built around the 4 K baseplate, directly below the LHe tank. (b) Photograph of the 4 K baseplate with major components labeled.

3.3 Synchronous tickle apparatus

In our experimental set-up, the helical resonator (used to step up the RF voltage) is directly connected to the trap RF electrodes, so the tickle signal must be added to the RF signal before it is input to the cryostat. The relatively low quality factor of the resonator (approximately 20) makes it possible to transmit the tickle signal in the form of sidebands at frequencies $\Omega_{RF} + \omega_{tickle}$ and $\Omega_{RF} - \omega_{tickle}$ without prohibitively high attenuation. Tickle detection proceeds using photons scattered on the Doppler cooling transition at 422 nm in $^{88}Sr^{+}$ (which has a linewidth of $\approx$ 20 MHz). A single laser beam at 422 nm passes across the trap at 45 degrees to the RF electrodes so that the two in-plane trap modes are both Doppler cooled. Photons emitted by the ion are collected using a high numerical aperture objective near the trap and converted to an electrical pulse train using a photomultiplier (PMT), which is then input to an FPGA-based (Opal Kelly XEM6001) photon counter for further processing. The components used to create the sidebands and perform tickle detection are diagrammed in Figure 3-4.

After transmission through mixer and couplers, the tickle signal applied by function generator 2 (see Figure 3-4) is attenuated by about 57 dB. The combined RF and tickle signals are amplified using an RF amplifier (Mini Circuits TIA-1000-1R8) followed by the helical resonator. Because the helical resonator is inaccessible from outside the chamber, the step-up it provides is not directly measurable. However, by measuring the secular frequencies (identifying the three motional sidebands present in spectroscopy of the qubit transition) and comparing with our trap model, the on-trap RF voltage, and hence the resonator step-up can be estimated. Using this method, the total voltage gain at the RF frequency (including the RF amplifier and the helical resonator) is found to be about 60 dB. Because the tickle signal is transmitted off-peak for the helical resonator, the gain is lower. By measuring the power reflection of the loaded resonator (using a bi-directional coupler), the full-width-half-maximum (FWHM) bandwidth is found to be approximately 1.2 MHz, meaning that at the tickle sideband frequency (around 1.2 MHz off peak) the gain is about 1/5 the peak value. So, for a voltage $V_{applied}$ by function generator 2, the resulting tickle voltage on the RF electrodes is about $0.27 \times V_{applied}$.

Both the PMT and the photon counter are phase-synchronized with the tickle voltage source (function generator 2 in Figure 3-4). The photon counter (which has an input buffer at 300 MHz), contains 275 separate counters which sum the leading edges of the PMT input (corresponding to single photons) over a chosen integration time. This makes it possible to average the PMT signal over many RF or tickle frequency cycles to increase the signal-to-noise ratio.

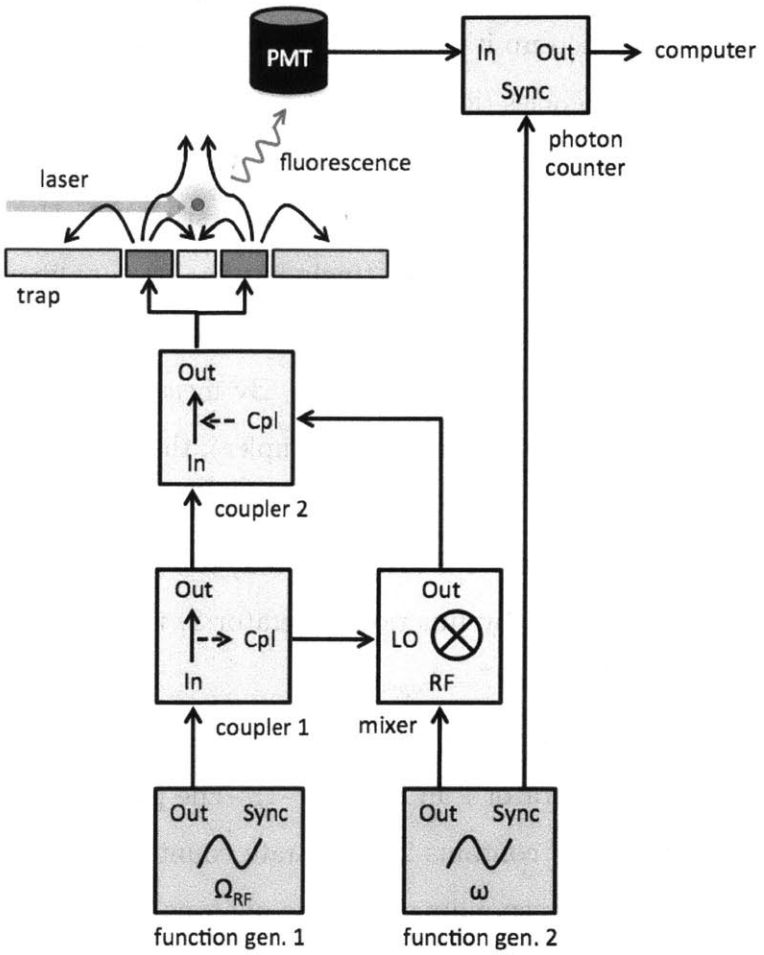

Figure 3-4: Schematic showing the apparatus for synchronous tickle detection. Function generator 1 provides the trap RF voltage at frequency Ω_{RF}, while function generator 2 provides the tickle signal at frequency ω. The first coupler (Mini Circuits ZDC-10-1-75+) draws a weak carrier signal to be mixed (Mini Circuits ZFM-3) with the tickle signal to produce sidebands at $\Omega_{RF}+\omega_{tickle}$ and $\Omega_{RF}-\omega_{tickle}$. These secular frequency sidebands are then fed from the mixer into the second coupler (also Mini Circuits ZDC-10-1-75+) to be added to the carrier (trap RF). The RF amplifier and helical resonator used to step up the output voltage before it is applied to the trap electrodes are not shown.

3.4 Experimental investigation

The synchronous tickle signal measured for an uncompensated trap can be seen in Figure 3-5. The qualitative features agree well with our theoretical model (see Figure 2-4). The tickle voltage applied at Function generator 2 (see Figure 3-4) was 100 mV (amplitude), corresponding to only $\approx$ 27 mV (amplitude) on trap. From the theoretical model developed in Section 2.4, the normalized amplitude measured (≈ 0.15) would correspond to an ion offset of about 5 μm from the RF null, or an uncompensated DC electric field of about 400 V/m. However, this model does not fully describe our experimental situation because the tickle voltage is not added in the form of a pure tone at frequency ω_{tickle}, but is instead added as amplitude modulation of the RF signal.

To compensate for ion offsets in the $\hat{y}$-direction (the direction out of the trap plane), we either add a small voltage (to move the ion away from the trap) or subtract a small voltage (to move the ion towards the trap) from all of the DC electrodes. Figure 3-6 shows how the synchronous tickle signal measured (the normalized amplitude on peak) changes as we scan the $\hat{y}$-compensation voltage with a tickle voltage of 200 mV (amplitude) applied. From the theoretical model developed in Section 2.4, the minimum normalized amplitude measured (≈ 0.14) would be caused by an ion offset of about 2.5 μm from the RF null, and the maximum normalized amplitude measured (≈ 0.23) would be caused by an ion offset of about 4.1 μm. From our trap model, the compensation voltage at the minimum ($\approx$ 0.14 V) corresponds to translating the ion by 2.1 μm in the $\hat{y}$-direction and the compensation voltage at the maximum ($\approx$ 0.3 V) corresponds to translating the ion by 4.5 μm. So, the two models are in approximate agreement.

The measurement sensitivity was limited by temperature fluctuations of the trap, which caused the impedance matching of the trap to the helical resonator, and hence the RF/tickle amplitude on trap, to vary in time, causing both the tickle signal amplitude and resonant frequency to fluctuate. This problem could be overcome by heat-sinking the trap electrodes to the 4 K baseplate of the cryostat more effectively.

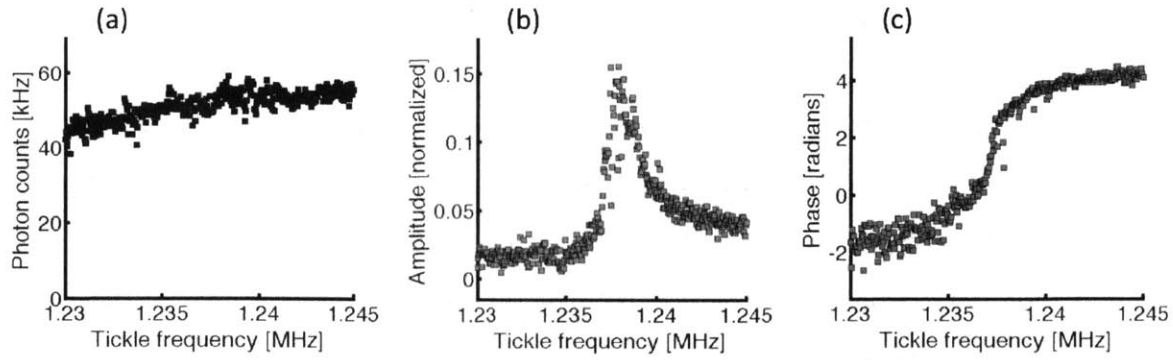

Figure 3-5: (a) Total photon scatter across the resonance (notice that there is no visible change in the total counts near the resonant frequency). (b) Correlated photon scatter (amplitude, normalized to the total scattering rate). (c) Correlated photon scatter (phase). The tickle voltage applied was 100 mV (amplitude) and the integration time was 500 ms.

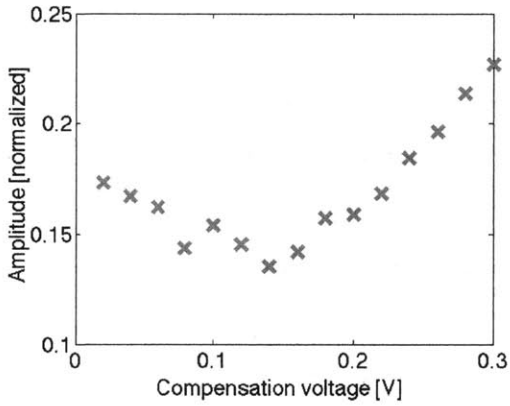

Figure 3-6: Peak correlated photon scatter (amplitude, normalized to the total scattering rate) for different compensation voltages. The tickle voltage applied was 200 mV (amplitude) and the integration time was 500 ms.

Instability of the DC voltage supplies may also have contributed to fluctuations in the resonant frequency. The DC voltage supplies also limited the compensation voltage resolution to about 1 mV (equivalent to $\approx$ 15 nm ion positioning resolution). Nonetheless, our experimental results verify that micromotion detection out-of-plane is possible using synchronous tickle measurement. Further work is needed to determine the ultimate sensitivity of the technique. In principle, a larger tickle voltage would result in a larger measurement resolution. However, if the ion is driven sufficiently hard by the applied tickle voltage, the amplitude of the ion's driven motion will cover a significant portion of the Doppler cooling beam waist, resulting in a change

in the cooling rate. If the ion is driven harder still, the amplitude of the ion's motion can take the ion outside of the trapping volume, and the trapped ion will be lost.

Chapter 4

Conclusion

This thesis has been motivated by recent demonstrations of quantum algorithms, error correction, and remote entanglement generation with a handful of trapped ion qubits. Our work has endeavored to develop the trap technology required to build these systems up to a scale where useful computation is possible. Surface-electrode ion traps show promise as the building block for a large-scale architecture, and so have been the focus of this work. The contributions of this thesis address the challenge of achieving sensitive micromotion compensation in all directions in a surface trap, difficult because laser beams typically cannot have a projection out of the trap plane (they cannot crash into the trap).

We have introduced a new technique for out-of-plane micromotion compensation, relying on synchronous detection of the driven secular motion of the ion when excited by sidebands on the trap RF drive. Combined with the RF correlation technique for micromotion compensation in-plane, our technique allows for sensitive, 3D micromotion compensation in a surface-electrode ion trap. Unlike other approaches, ours does not require access to a narrow atomic transition or require a laser beam crashing into the trap surface, which make it widely applicable. In theory, the measurement sensitivity should be such that micromotion compensation to within the ground state wavepacket size of the trapped ion is possible within milli-seconds. More generally, our technique allows a trapped ion to serve as a sensitive probe of DC electric fields.

We have verified our technique experimentally with a single $^{88}Sr^{+}$ ion confined

150 μm above a surface-electrode ion trap, cooled by contact to the 4 K baseplate of a bath cryostat. Our measurement sensitivity was limited by temperature fluctuations of the trap, and by the precision and stability of the DC supplies used to set the trap voltages. This first issue could be mitigated by better heat-sinking the trap to the 4 K baseplate of the cryostat, and the second issue could be addressed by building better DC supplies (a new DAC system). With these in hand, it will be possible to experimentally determine the ultimate sensitivity of our technique.

Bibliography

Following each bibliography item, pages in the text referring to the item are listed:

[ASA+09] P. B. Antohi, D. Schuster, G. M. Akselrod, J. Labaziewicz, Y. Ge, Z. Lin, W. S. Bakr, and I. L. Chuang. Cryogenic ion trapping systems with surface-electrode traps. *Review of Scientific Instruments*, 80(1):013103, January 2009. 37

[ASS+10] D. T. C. Allcock, J. A. Sherman, D. N. Stacey, A. H. Burrell, M. J. Curtis, G. Imreh, N. M. Linke, D. J. Szwer, S. C. Webster, a. M. Steane, and D. M. Lucas. Implementation of a symmetric surface-electrode ion trap with field compensation using a modulated Raman effect. *New Journal of Physics*, 12(5):053026, May 2010. 19, 21

[Bak06] W. Bakr. *Towards a Cryogenic Planar Ion Trap for Sr-88.* Bachelors thesis, Massachusetts Institute of Technology, 2006. 37

[BHL+05] K. A. Brickman, P. Haljan, P. Lee, M. Acton, L. Deslauriers, and C. Monroe. Implementation of Grovers quantum search algorithm in a scalable system. *Physical Review A*, 72(5):050306, November 2005. 14

[BKQW89] R. Blümel, C. Kappler, W. Quint, and H. Walther. Chaos and order of laser-cooled ions in a Paul trap. *Physical Review A*, 40(2):808–823, 1989. 17

[BLW+07] M. Brownnutt, V. Letchumanan, G. Wilpers, R. Thompson, P. Gill, and a.G. Sinclair. Controlled photoionization loading of 88Sr+ for precision ion-trap experiments. *Applied Physics B*, 87(3):411–415, May 2007. 17

[BM98] D. Berkeland and J. Miller. Minimization of ion micromotion in a Paul trap. *Journal of Applied Physics*, 83(10):5025–5033, 1998. 15, 17, 18, 19, 25, 28

[CBB+05] J. Chiaverini, R. B. Blakestad, J. Britton, J. D. Jost, C. Langer, D. Leibfried, R. Ozeri, and D. J. Wineland. Surface-electrode architecture for ion-trap quantum information processing. *Quantum Information & Computation*, 5(6):419–439, September 2005. 24

[CBL+05] J. Chiaverini, J. Britton, D. Leibfried, E. Knill, M. D. Barrett, R. B. Blakestad, W. M. Itano, J. D. Jost, C. Langer, R. Ozeri, T. Schaetz, and D. J. Wineland. Implementation of the semiclassical quantum Fourier transform in a scalable system. *Science*, 308(5724):997–1000, May 2005. 14

[CGV12] M. Cetina, A. T. Grier, and V. Vuletić. Micromotion-Induced Limit to Atom-Ion Sympathetic Cooling in Paul Traps. *Physical Review Letters*, 109(25):253201, December 2012. 18

[DHB89] R. DeVoe, J. Hoffnagle, and R. Brewer. Role of laser damping in trapped ion crystals. *Physical Review A*, 39(9):4362–4366, 1989. 17, 26

[DiV95] D. DiVincenzo. Quantum computation. *Science*, 270(5234):255–261, 1995. 14

[DMM+04] M. Drewsen, a. Mortensen, R. Martinussen, P. Staanum, and J. Sø rensen. Nondestructive Identification of Cold and Extremely Localized Single Molecular Ions. *Physical Review Letters*, 93(24):1–4, December 2004. 22

[GRL+03] S. Gulde, M. Riebe, G. P. T. Lancaster, C. Becher, J. Eschner, H. Häffner, F. Schmidt-Kaler, I. L. Chuang, and R. Blatt. Implementation of the Deutsch-Jozsa algorithm on an ion-trap quantum computer. *Nature*, 421(6918):48–50, January 2003. 14

[Gro96] L. Grover. A fast quantum mechanical algorithm for database search. In *Proceedings, 28th Annual ACM Symposium on the Theory of Computing (STOC)*, pages 212–219, 1996. 14

[HHJ+09] J. P. Home, D. Hanneke, J. D. Jost, J. M. Amini, D. Leibfried, and D. J. Wineland. Complete methods set for scalable ion trap quantum information processing. *Science*, 325(5945):1227–1230, September 2009. 14

[Hou08] M. House. Analytic model for electrostatic fields in surface-electrode ion traps. *Physical Review A*, 78(033402), September 2008. 30

[IUZ+10] L. Isenhower, E. Urban, X. L. Zhang, a. T. Gill, T. Henage, T. a. Johnson, T. G. Walker, and M. Saffman. Demonstration of a Neutral Atom Controlled-NOT Quantum Gate. *Physical Review Letters*, 104(1):010503, January 2010. 14

[KHC11] T. H. Kim, P. F. Herskind, and I. L. Chuang. Surface-electrode ion trap with integrated light source. *Applied Physics Letters*, 98(21):214103, 2011. 17

[KMW02] D. Kielpinski, C. Monroe, and D. J. Wineland. Architecture for a large-scale ion-trap quantum computer. *Nature*, 417(6890):709–711, June 2002. 9, 15, 17

[KWM+98] B. King, C. Wood, C. Myatt, Q. Turchette, D. Leibfried, W. Itano, C. Monroe, and D. Wineland. Cooling the Collective Motion of Trapped Ions to Initialize a Quantum Register. *Physical Review Letters*, 81(7):1525–1528, August 1998. 14

[LDM+03] D. Leibfried, B. DeMarco, V. Meyer, D. Lucas, M. Barrett, J. Britton, W. M. Itano, B. Jelenković, C. Langer, T. Rosenband, and D. J. Wineland. Experimental demonstration of a robust, high-fidelity geometric two ion-qubit phase gate. *Nature*, 422(6930):412–415, March 2003. 14

[LGA+08] J. Labaziewicz, Y. Ge, P. Antohi, D. Leibrandt, K. Brown, and I. Chuang. Suppression of Heating Rates in Cryogenic Surface-Electrode Ion Traps. *Physical Review Letters*, 100(1):013001, January 2008. 22, 37

[MKH+09] T. Monz, K. Kim, W. Hänsel, M. Riebe, a. Villar, P. Schindler, M. Chwalla, M. Hennrich, and R. Blatt. Realization of the Quantum Toffoli Gate with Trapped Ions. *Physical Review Letters*, 102(4):040501, January 2009. 14

[MMK95a] C. Monroe, D. Meekhof, and B. King. Demonstration of a fundamental quantum logic gate. *Physical Review Letters*, 75(25):4714–4717, 1995. 14

[MMK95b] C. Monroe, D. M. Meekhof, and B. E. King. Resolved-Sideband Raman Cooling of a Bound Atom to the 3D Zero-Point Energy. *Physical Review Letters*, 75(22):4011–4014, 1995. 14

[MSB+11] T. Monz, P. Schindler, J. Barreiro, M. Chwalla, D. Nigg, W. Coish, M. Harlander, W. Hänsel, M. Hennrich, and R. Blatt. 14-Qubit Entanglement: Creation and Coherence. *Physical Review Letters*, 106(13):1–4, March 2011. 14

[MSW+08] A. Myerson, D. Szwer, S. Webster, D. Allcock, M. Curtis, G. Imreh, J. Sherman, D. Stacey, A. Steane, and D. Lucas. High-Fidelity Readout of Trapped-Ion Qubits. *Physical Review Letters*, 100(20):2–5, May 2008. 14

[NDM+11] S. Narayanan, N. Daniilidis, S. a. Moller, R. Clark, F. Ziesel, K. Singer, F. Schmidt-Kaler, and H. Haffner. Electric field compensation and sens-

ing with a single ion in a planar trap. *Journal of Applied Physics*, 110(11):114909, 2011. 20, 21

[NLR+99] H. Nägerl, D. Leibfried, H. Rohde, G. Thalhammer, J. Eschner, F. Schmidt-Kaler, and R. Blatt. Laser addressing of individual ions in a linear ion trap. *Physical Review A*, 60(1):145–148, July 1999. 14

[PJT+05] J. R. Petta, A. C. Johnson, J. M. Taylor, E. A. Laird, A. Yacoby, M. D. Lukin, C. M. Marcus, M. P. Hanson, and A. C. Gossard. Coherent manipulation of coupled electron spins in semiconductor quantum dots. *Science (New York, N.Y.)*, 309(5744):2180–4, September 2005. 14

[PMO09] A. Politi, J. C. F. Matthews, and J. L. O'Brien. Shor's quantum factoring algorithm on a photonic chip. *Science (New York, N.Y.)*, 325(5945):1221, September 2009. 14

[RDN+12] M. D. Reed, L. DiCarlo, S. E. Nigg, L. Sun, L. Frunzio, S. M. Girvin, and R. J. Schoelkopf. Realization of three-qubit quantum error correction with superconducting circuits. *Nature*, 482(7385):382–385, February 2012. 14

[RKMS01] M. A. Rowe, D. Kielpinski, V. Meyer, and C. A. Sackett. Experimental violation of a Bell's inequality with efficient detection. *Nature*, 409:791–794, 2001. 14

[Roo00] C. Roos. *Controlling the quantum state of trapped ions.* Doctoral thesis, University of Innsbruck, 2000. 18, 19, 21

[RZR+99] C. Roos, T. Zeiger, H. Rohde, H. Nägerl, J. Eschner, D. Leibfried, F. Schmidt-Kaler, and R. Blatt. Quantum State Engineering on an Optical Transition and Decoherence in a Paul Trap. *Physical Review Letters*, 83(23):4713–4716, December 1999. 14

[RZS05] V. Ryjkov, X. Zhao, and H. Schuessler. Simulations of the rf heating rates in a linear quadrupole ion trap. *Physical Review A*, 71(3):033414, March 2005. 17

[SBM+11] P. Schindler, J. T. Barreiro, T. Monz, V. Nebendahl, D. Nigg, M. Chwalla, M. Hennrich, and R. Blatt. Experimental repetitive quantum error correction. *Science*, 332(6033):1059–61, May 2011. 14

[SCR+06] S. Seidelin, J. Chiaverini, R. Reichle, J. Bollinger, D. Leibfried, J. Britton, J. Wesenberg, R. Blakestad, R. Epstein, D. Hume, W. Itano, J. Jost, C. Langer, R. Ozeri, N. Shiga, and D. Wineland. Microfabricated Surface-Electrode Ion Trap for Scalable Quantum Information Processing. *Physical Review Letters*, 96(25):1–4, June 2006. 15

[Sho94] P. Shor. Algorithms for quantum computation: discrete logarithms and factoring. In *Proc. 35nd Annual Symposium on Foundations of Computer Science*, pages 124–134, 1994. 14

[SHO+05] D. Stick, W. K. Hensinger, S. Olmschenk, M. J. Madsen, K. Schwab, and C. Monroe. Ion trap in a semiconductor chip. *Nature Physics*, 2(1):36–39, December 2005. 15

[SKHR+03] F. Schmidt-Kaler, H. Häffner, M. Riebe, S. Gulde, G. P. T. Lancaster, T. Deuschle, C. Becher, C. F. Roos, J. Eschner, and R. Blatt. Realization of the Cirac-Zoller controlled-NOT quantum gate. *Nature*, 422(6930):408–411, March 2003. 14

[SKK+00] C. A. Sackett, D. Kielpinski, B. E. King, C. Langer, V. Meyer, C. J. Myatt, M. Rowe, Q. A. Turchette, W. M. Itano, D. J. Wineland, and C. Monroe. Experimental entanglement of four particles. *Nature*, 404(6775):256–9, March 2000. 14

[TKL+00] Q. a. Turchette, B. E. King, D. Leibfried, D. M. Meekhof, C. J. Myatt, M. a. Rowe, C. a. Sackett, C. S. Wood, W. M. Itano, C. Monroe, and

D. J. Wineland. Heating of trapped ions from the quantum ground state. *Physical Review A*, 61(6):1–8, May 2000. 15

[TMA+11] U. Tanaka, K. Masuda, Y. Akimoto, K. Koda, Y. Ibaraki, and S. Urabe. Micromotion compensation in a surface electrode trap by parametric excitation of trapped ions. *Applied Physics B*, 107(4):907–912, October 2011. 20

[VSB+00] L. M. Vandersypen, M. Steffen, G. Breyta, C. S. Yannoni, R. Cleve, and I. L. Chuang. Experimental realization of an order-finding algorithm with an NMR quantum computer. *Physical Review Letters*, 85(25):5452–5455, December 2000. 14

[WHL+11] S. X. Wang, G. Hao Low, N. S. Lachenmyer, Y. Ge, P. F. Herskind, and I. L. Chuang. Laser-induced charging of microfabricated ion traps. *Journal of Applied Physics*, 110(10):104901, 2011. 15, 17

[WLG+10] S. Wang, J. Labaziewicz, Y. Ge, R. Shewmon, and I. Chuang. Demonstration of a quantum logic gate in a cryogenic surface-electrode ion trap. *Physical Review A*, 81(6):062332, June 2010. 26

[WMI+98] D. Wineland, C. Monroe, W. Itano, D. Leibfried, B. King, and D. Meekhof. Experimental issues in coherent quantum-state manipulation of trapped atomic ions. *Journal of Research of the National Institute of Standards and Technology*, 103(3):259, May 1998. 14